


RESEARCH

Open Access



A core-shell Au@Cu_{2-x}Se heterogeneous metal nanocomposite for photoacoustic and computed tomography dual-imaging-guided photothermal boosted chemodynamic therapy

Le Zhang^{1,3,4}, Chunjuan Jiang¹, Bing Li^{2,3,4}, Zhengwang Liu^{1,3,4}, Bingxin Gu¹, Simin He¹, Panli Li¹, Yun Sun^{1,2,3,4*} and Shaoli Song^{1,3,4*} 

Abstract

Chemodynamic therapy (CDT) has aroused extensive attention for conquering cancers because of its high specificity and low invasiveness. Quick generation of hydroxyl radicals ($\cdot\text{OH}$) during CDT could induce more irreparable damage to cancer cells. The generation rate of $\cdot\text{OH}$ could be magnified via the selection of suitable nanocatalysts or under the assistance of exogenous thermal energy from photothermal therapy (PTT). Here, we construct a kind of mono-disperse core-shell Au@Cu_{2-x}Se heterogeneous metal nanoparticles (NPs) for PTT boosted CDT synergistic therapy. Due to the localized surface plasmon resonance (LSPR) coupling effect in the core-shell structure, the photothermal conversion efficiency of Au@Cu_{2-x}Se NPs is up to 56.6%. The in situ generated heat from photothermal can then accelerate the Fenton-like reaction at Cu⁺ sites to produce abundant $\cdot\text{OH}$, which will induce apoptotic cell death by attacking DNA, contributing to a heat-boosted CDT. Both in vitro and in vivo results showed that after this synergistic therapy, tumors could be remarkably suppressed. Guided by photoacoustic (PA) and computed tomography (CT) imaging, the therapeutic effects were more specified. Our results revealed that PA and CT dual-imaging-guided PTT boosted CDT synergistic therapy based on core-shell Au@Cu_{2-x}Se NPs is an effective cancer treatment strategy.

Keywords: Chemodynamic therapy, Photothermal therapy, Core-shell metal nanoparticles, Fenton-like reaction, Tumor imaging

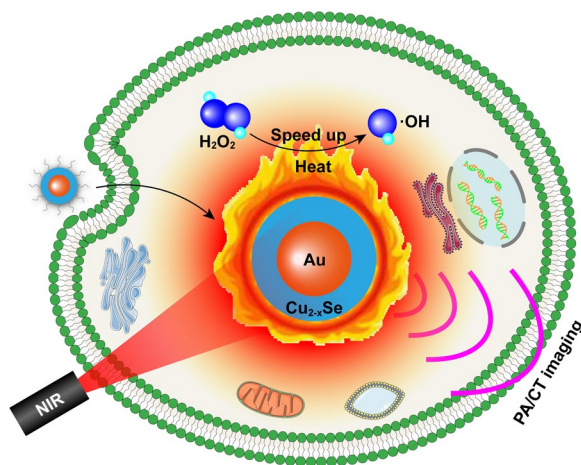
*Correspondence: yun.sun@sphic.org.cn; shaoli-song@163.com

¹ Department of Nuclear Medicine, Shanghai Proton and Heavy Ion Center, Fudan University Cancer Hospital, Shanghai 201321, China
Full list of author information is available at the end of the article



© The Author(s) 2021. **Open Access** This article is licensed under a Creative Commons Attribution 4.0 International License, which permits use, sharing, adaptation, distribution and reproduction in any medium or format, as long as you give appropriate credit to the original author(s) and the source, provide a link to the Creative Commons licence, and indicate if changes were made. The images or other third party material in this article are included in the article's Creative Commons licence, unless indicated otherwise in a credit line to the material. If material is not included in the article's Creative Commons licence and your intended use is not permitted by statutory regulation or exceeds the permitted use, you will need to obtain permission directly from the copyright holder. To view a copy of this licence, visit <http://creativecommons.org/licenses/by/4.0/>. The Creative Commons Public Domain Dedication waiver (<http://creativecommons.org/publicdomain/zero/1.0/>) applies to the data made available in this article, unless otherwise stated in a credit line to the data.

Graphical Abstract



Introduction

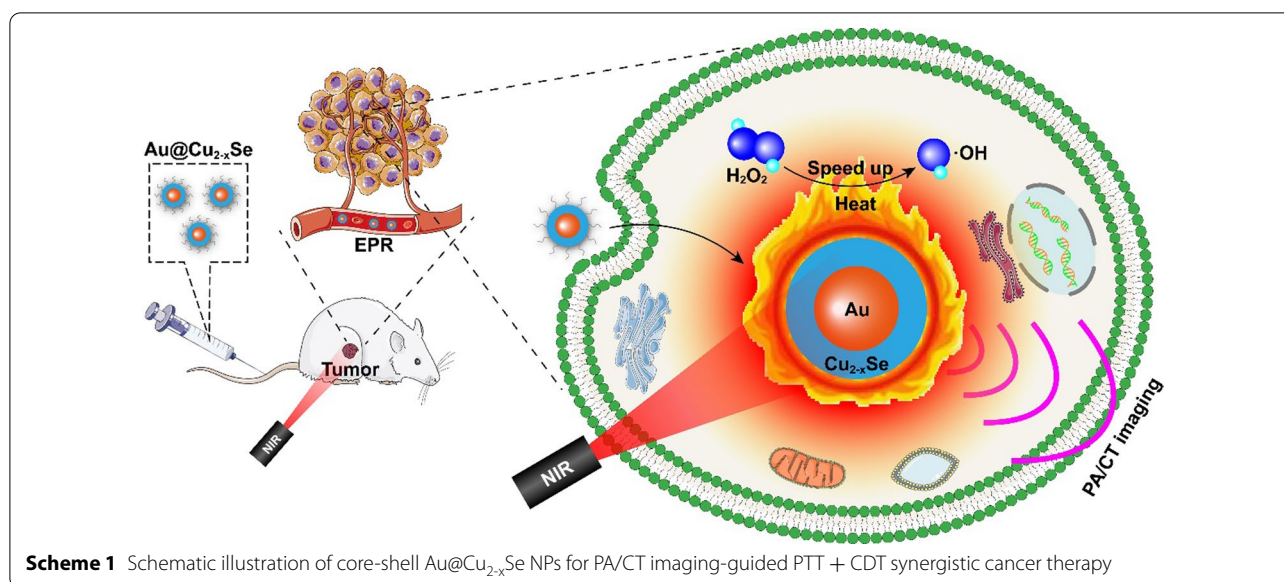
Reactive oxygen species (ROS), mainly including hydrogen peroxide (H₂O₂), singlet oxygen (¹O₂), superoxide anion (O₂^{•-}), and hydroxyl radical (·OH), have significant influences on various physiological functions of cancer cells. At moderate levels, ROS could facilitate cancer occurrence and development either by inducing the mutation of genomic DNA or by acting as pro-oncogenic signaling molecules. At high levels, ROS can cause severe damage and death of cancer cells via attacking cellular components such as lipids, proteins, and DNA [1–3]. Therefore, upregulating the ROS levels in cancer cells represents a promising strategy for cancer therapy. Among various ROS-enhanced anticancer strategies, chemodynamic therapy (CDT), which uses Fenton or Fenton-like reaction catalyzed by nanomaterials to decompose less-reactive H₂O₂ overexpressed in tumor cells into highly cytotoxic ·OH, is an emerging therapeutic route because of the merits of high therapeutic specificity and low invasiveness [4, 5]. However, the sluggish Fenton kinetics result in the unsatisfactory efficacy of CDT, because the generation rate of ·OH is not quick enough to overcome the intracellular antioxidant system. Therefore, how to speed up the sluggish Fenton kinetics is a major concern for CDT at present.

Nanocatalysts play an irreplaceable role in CDT. Fe²⁺-based nanomaterials are the widely exploited nanocatalysts for CDT, such as Fe₃O₄ nanoparticles [6], Fe₂P nanorods [7], and FePS₃ nanosheets [8]. However, Fe²⁺-based nanomaterials only exhibit high Fenton catalytic activity in low pH conditions (pH 2–4). The weakly acid tumor microenvironment (TME, pH ~6.5) is not conducive to Fe²⁺-based nanomaterials [9]. It has been reported that Cu⁺-catalyzed Fenton-like reactions

are easier to occur in weakly acidic and neutral media, compared with Fe²⁺-catalyzed Fenton reactions [9]. So Cu⁺-containing catalysts may be a better candidate.

Stimulation by external energy fields, such as heat, light, and ultrasound, is more workable to speed up Fenton kinetics to improve CDT effects [4, 5]. Photothermal therapy (PTT) based on nanomaterials is another effective but less invasive therapeutic alternative, which converts near-infrared (NIR) light into local heat to realize tumor ablation. The hyperthermia generated in PTT can not only kill cancer cells but also speed up the Fenton-like reaction in CDT, consequently achieving a synergistic therapeutic outcome [8, 10, 11]. It has been reported that by constructing Au@semiconductor core-shell dual plasmonic hybrid nanocomposite, the photothermal conversion efficiency of nanocomposite could be efficiently improved because the core-shell structure could couple the localized surface plasmon resonance (LSPR) of two components to a maximum degree [12–14]. So introducing Au into Cu⁺-based nanomaterials can simultaneously achieve PTT and CDT in a single platform. Besides, both photoacoustic (PA) imaging and PTT depend on a similar NIR absorption mechanism, plus Au has computed tomography (CT) imaging property due to its X-ray attenuation capability, so PA/CT dual-imaging guided PTT + CDT synergistic therapy will be realized.

Herein, we developed a kind of monodisperse core-shell Au@Cu_{2-x}Se hybrid metal nanoparticles (NPs) as a multifunctional theranostic nanoplatform for PA/CT dual-imaging-guided combinational tumor therapy of PTT and the boosted CDT (Scheme 1). The core-shell structure strengthens the LSPR coupling between Au and Cu_{2-x}Se and thus heightens the overall photothermal conversion efficiency of Au@Cu_{2-x}Se NPs. The existence



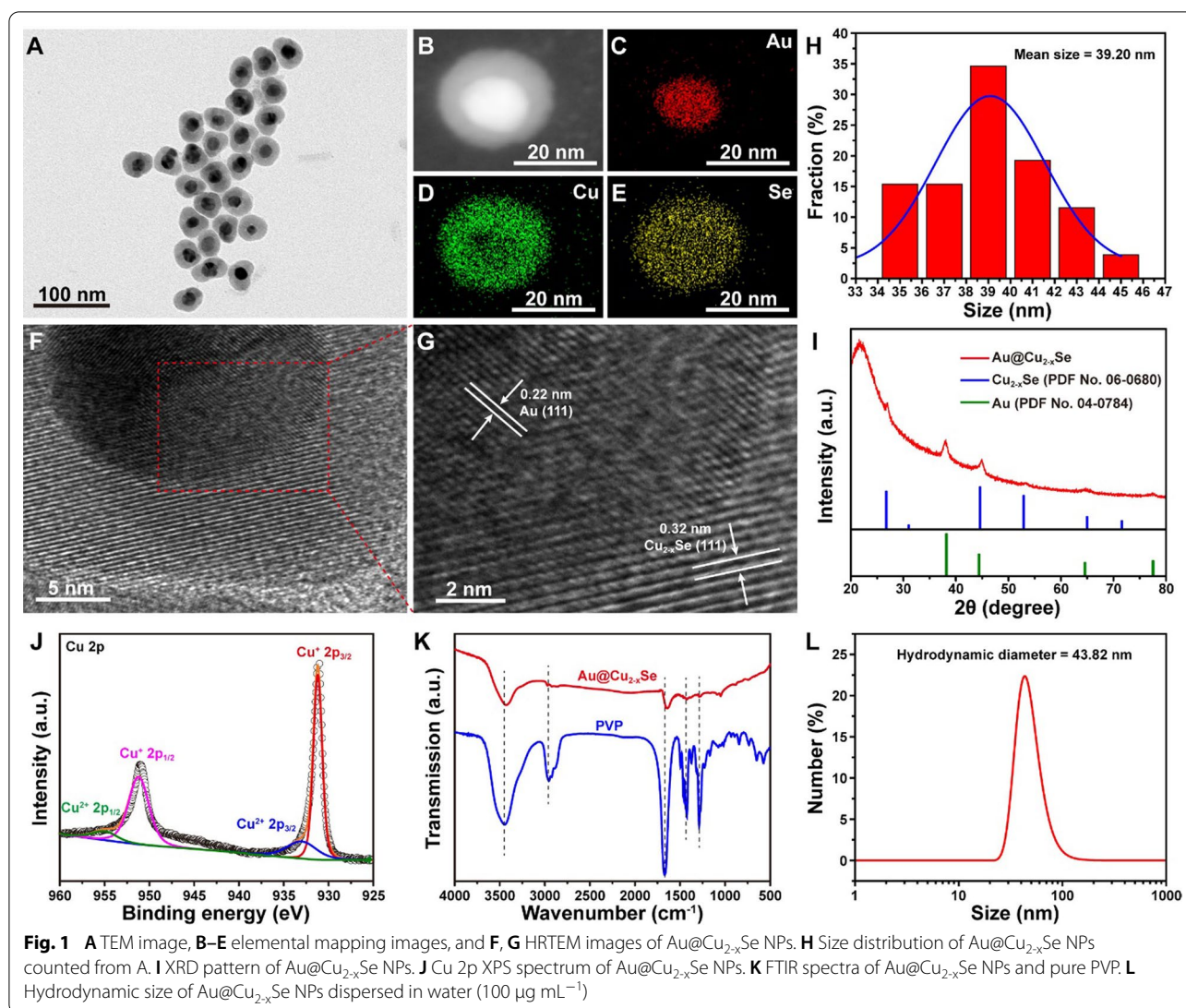
of Cu⁺ enables high Fenton-like catalytic activity of Au@Cu_{2-x}Se NPs for CDT. More importantly, the Fenton-like reaction at Cu⁺ sites can be accelerated by the in situ generated heat from PTT, wherein the produced ·OH will cause DNA breaks and then initiate cell apoptosis. Finally, the quick hyperthermia by PTT and quick production of ·OH by the boosted CDT defeat the intracellular antioxidant systems and induce irreversible damage to tumor cells. In addition, Au@Cu_{2-x}Se NPs have the potential as a contrast agent for PA and CT imaging, which could make this combinational therapy more specified. The heterogeneous metal nanocomposite paves the way of precisely controlling the reactive oxygen microenvironment in tumor to inhibit tumor progression.

Results and discussion

Synthesis and characterization of Au@Cu_{2-x}Se NPs

Monodisperse core-shell Au@Cu_{2-x}Se NPs were prepared via an eco-friendly two-step procedure. Au cores were first obtained by reducing HAuCl₄ with sodium citrate. Subsequently, Cu_{2-x}Se grew onto the Au surface by co-reducing Cu²⁺ and SeO₂ with ascorbic acid (Additional file 1: Fig. S1) under the assistance of polyvinylpyrrolidone (PVP). Transmission electron microscope (TEM) image (Fig. 1A, H) demonstrates the core-shell structure of Au@Cu_{2-x}Se with an average size of 39.20 nm. Corresponding element mapping (Fig. 1B–E) confirms that Cu and Se are uniformly distributed around the Au core. The measured lattice distances of core and shell from high-resolution TEM image (HRTEM, Fig. 1F, G) are 0.22 and 0.32 nm, which correspond to the (111) plane of Au and (111) plane of

Cu_{2-x}Se [15, 16], respectively. The selected area electron diffraction (SAED) pattern (Additional file 1: Fig. S2) reveals that Au@Cu_{2-x}Se NPs are highly crystalline. X-ray diffraction (XRD) pattern (Fig. 1I) proves the formation of cubic phase Au (PDF No. 04-0784) and cubic berzelianite phase Cu_{2-x}Se (PDF No. 06-0680). X-ray photoelectron spectroscopy (XPS) was then performed to analyze the chemical compositions of Au@Cu_{2-x}Se. In the high-resolution Cu 2p XPS spectra (Fig. 1J), the peaks at 931.2 and 951.2 eV can be attributed to the Cu⁺ state, and the peaks at 933.0 and 955.0 eV is related to the Cu²⁺ state [16]. The peak area of Cu⁺ is larger than that of Cu²⁺, indicating that Cu mainly exists as Cu⁺. This ensures the good catalytic activity of Au@Cu_{2-x}Se for Fenton-like reaction because Cu⁺ has better activity than Cu²⁺ [9, 17]. N 1s XPS spectrum (Additional file 1: Fig. S3) implies the coating of PVP on Au@Cu_{2-x}Se surface. This can be further substantiated by Fourier transform infrared (FTIR) spectra (Fig. 1K), wherein Au@Cu_{2-x}Se presents the four characteristic absorption bands of PVP at 1289, 1426, 1664, and 2957 cm⁻¹, respectively [18, 19]. The modification with PVP endows Au@Cu_{2-x}Se proper zeta potential (−24.51 mV, Additional file 1: Fig. S4) and good biocompatibility in physiological conditions. The hydrodynamic size of Au@Cu_{2-x}Se determined by dynamic light scattering (DLS) is around 43.82 nm (Fig. 1L), which is suitable for biomedical applications. Besides, the morphology of Au@Cu_{2-x}Se NPs after 14-day incubation either in saline or in RPMI-1640 complete medium has no obvious changes (Additional file 1: Fig. S5), indicating the excellent stability of Au@Cu_{2-x}Se NPs for durable therapy.

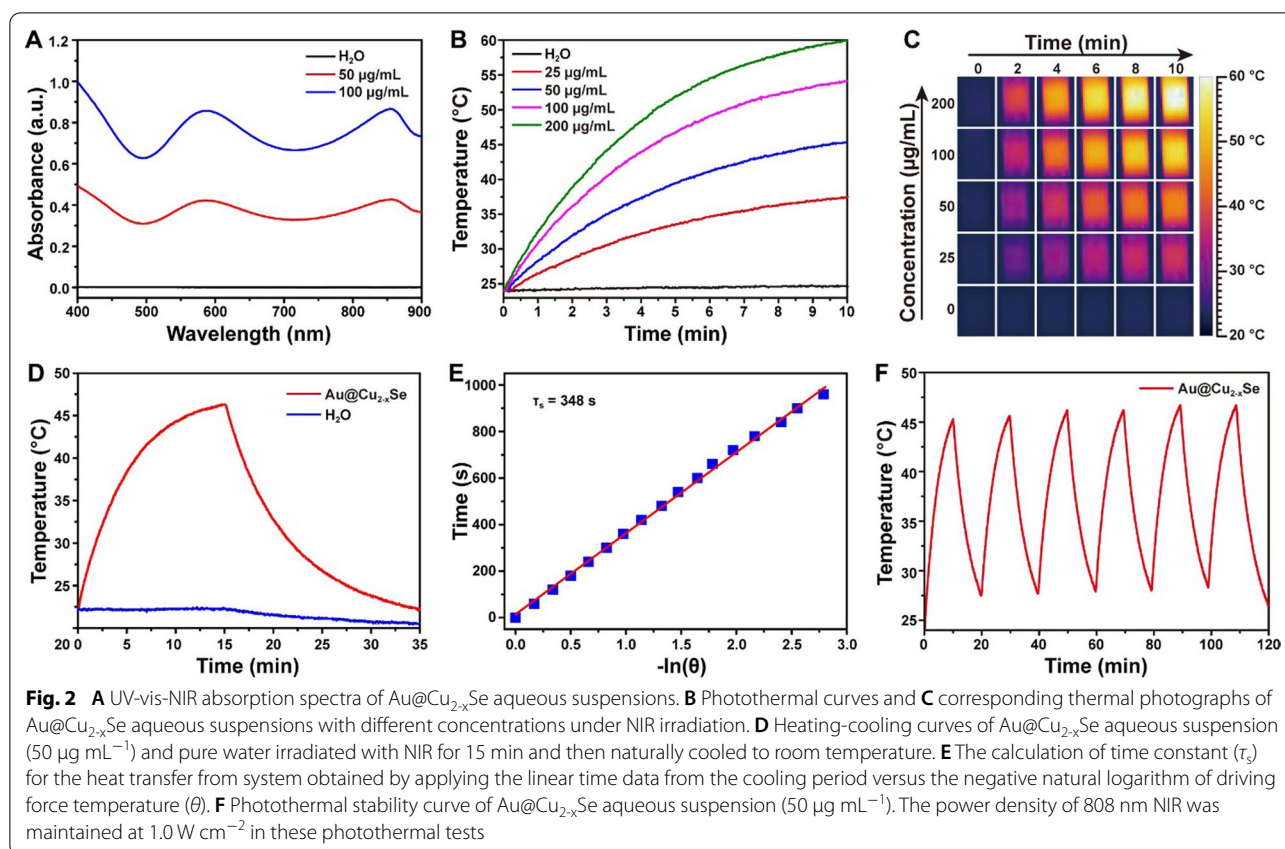


Photothermal performance of Au@Cu_{2-x}Se NPs

Ultraviolet-visible-infrared (UV-vis-NIR) absorption spectra (Fig. 2A) revealed that Au@Cu_{2-x}Se NPs aqueous suspensions possessed strong absorption in NIR region, implying the potential as a nanoagent for PTT. To investigate the detailed photothermal performance, the Au@Cu_{2-x}Se NPs aqueous suspensions with different concentrations were exposed to an 808 nm NIR laser at a power density of 1.0 W cm⁻². Significant concentration-dependent temperature increases of solutions were observed under laser irradiation (Fig. 2B, C). For example, 10 min NIR irradiation for 50 μg mL⁻¹ solution induced a quick heat from room temperature to 45 °C. In contrast, the temperature of pure water had negligible change under identical laser condition. The calculated photothermal conversion efficiency of Au@Cu_{2-x}Se NPs was about 56.6% (Fig. 2D, E), which is much superior to

most recently reported materials, such as Au-Fe₂C nanoparticles (30.2%) [20], PVP-Bi nanodots (30%) [21], V₂C nanosheets (48%) [22], NbSe₂ nanosheets (42.9%) [23] (see details in Additional file 1: Table S1). To evaluate the photothermal stability of Au@Cu_{2-x}Se NPs, the temperature variation of Au@Cu_{2-x}Se NPs dispersion was recorded under six cycles of heating and cooling process upon NIR laser exposure. There was little deterioration of photothermal performance during each cycle (Fig. 2F), illustrating that Au@Cu_{2-x}Se NPs have a durable therapeutic efficiency for PTT.

To identify the role of core-shell structure in the photothermal conversion, the photothermal performance of Au@Cu_{2-x}Se NPs was compared with that of individual Au NPs and individual Cu_{2-x}Se NPs. TEM characterizations confirm the successful preparation of Au NPs (Additional file 1: Fig. S6) and Cu_{2-x}Se NPs (Additional



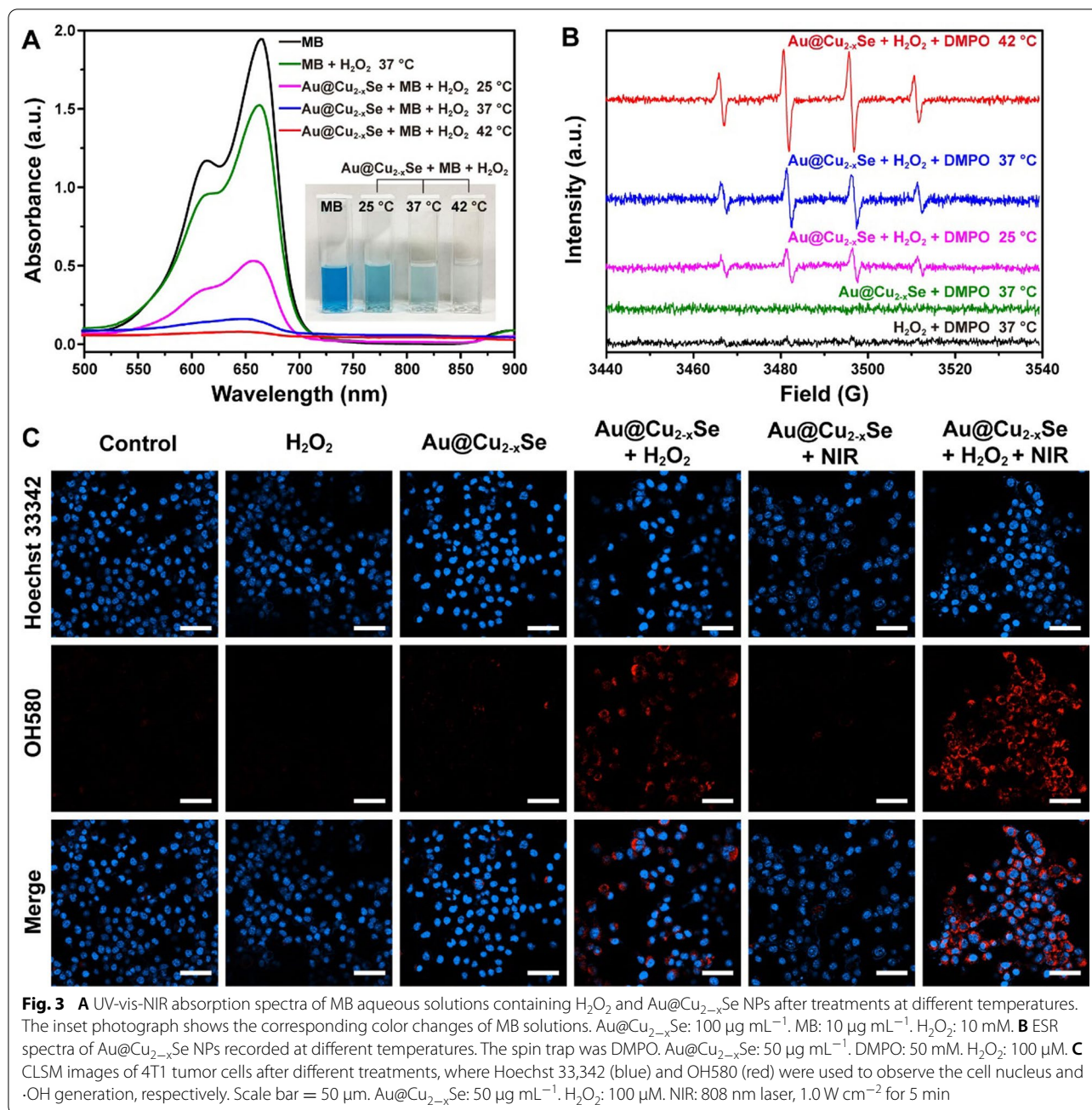
file 1: Fig. S7). As shown in Additional file 1: Fig. S8, the absorbance of Au@Cu_{2-x}Se NPs at 808 nm was higher than that of Au NPs, Cu_{2-x}Se NPs, and physical mixture of Au NPs and Cu_{2-x}Se NPs (Additional file 1: Fig. S8A, C). The temperature increase rate of Au@Cu_{2-x}Se NPs dispersion was also faster than that of Au NPs, Cu_{2-x}Se NPs, and physical mixture of Au NPs and Cu_{2-x}Se NPs dispersion (Additional file 1: Fig. S8B, D). Based on these results and combined with previous reports, such high photothermal property of Au@Cu_{2-x}Se NPs can be attributed to its unique core-shell structure. Combining the Au metal and Cu_{2-x}Se semiconductor into one core-shell hybrid nanocomposite could achieve a strong LSPR coupling between Au and Cu_{2-x}Se and thus enhance the NIR absorption, consequently leading to the improved photothermal effect [12–14].

Photothermal enhanced Fenton-like catalytic activity of Au@Cu_{2-x}Se NPs

The therapeutic efficiency of CDT depends on the generation rate of $\cdot\text{OH}$ in the Fenton-like reaction. The existence of Cu⁺ theoretically proves that Au@Cu_{2-x}Se NPs have Fenton-like activity [9, 17]. Degradation experiments of methylene blue (MB) were then carried out to evaluate the heat-enhanced Fenton-like activity of Au@

Cu_{2-x}Se NPs. After incubating MB with Au@Cu_{2-x}Se NPs at 25, 37, or 42 °C for 30 min in water containing H₂O₂, the absorbance of supernatant was measured, where the absorbance decrease at 664 nm was induced by $\cdot\text{OH}$ radical. The temperature-dependent MB degradation is shown in Fig. 3A. A slight decrease of absorbance in MB + H₂O₂ group was observed, implying that H₂O₂ might degrade part of MB. More significant decrease of absorbance in Au@Cu_{2-x}Se + MB + H₂O₂ groups was observed, and the extent of decrease increased with the increase of temperature. The absorbance at 42 °C was 7.43 times lower than that at 25 °C. These results manifest that thermal energy could indeed accelerate $\cdot\text{OH}$ production. A similar temperature-dependent MB degradation phenomenon was also observed on pure Cu_{2-x}Se NPs (Additional file 1: Fig. S9), indicating that the Fenton-like catalytic activity of Au@Cu_{2-x}Se NPs derives from Cu_{2-x}Se shell. Of course, MB degradation could also be achieved by prolonging the reaction time (Additional file 1: Fig. S10), but this is not the optimal strategy.

The generation of $\cdot\text{OH}$ at different temperatures was then detected via electron spin resonance (ESR) by using 5,5-dimethyl-1-pyrroline N-oxide (DMPO) as a spin trap. DMPO captures short-lived $\cdot\text{OH}$ radicals to form relatively long-lived DMPO-OH adducts, which exhibit



typical four peaks with relative intensities of 1:2:2:1 in ESR spectrum [24, 25]. As shown in Fig. 3B, compared with H_2O_2 or $Au@Cu_{2-x}Se$ alone, $Au@Cu_{2-x}Se + H_2O_2$ group exhibited higher ESR signal and DMPO-OH characteristic peaks. Meanwhile, higher characteristic signal peaks could be recognized at higher temperatures, supporting the enhancing effect of thermal energy toward Fenton-like reaction catalyzed by $Au@Cu_{2-x}Se$ NPs.

Based on above results, the photothermal accelerated $\cdot OH$ generation in Fenton-like reaction catalyzed

by $Au@Cu_{2-x}Se$ NPs was verified. As expected, under 10 min of NIR irradiation at $1.0 W cm^{-2}$, the temperature of mixed solution of $Au@Cu_{2-x}Se$ NPs ($100 \mu g mL^{-1}$), MB, and H_2O_2 increased from room temperature to $58^\circ C$ (Additional file 1: Fig. S11A). After removing $Au@Cu_{2-x}Se$ NPs, the supernatant became colorless, and its absorbance was reduced by 99% (Additional file 1: Fig. S11B, C). This result further validates the feasibility of using photothermal to enhance CDT based on $Au@Cu_{2-x}Se$ NPs.

In vitro photothermal and chemodynamic therapy based on Au@Cu_{2-x}Se NPs

Before executing the anticancer effect of Au@Cu_{2-x}Se NPs via PTT + CDT in vitro, confocal laser scanning microscope (CLSM) was adopted to show the production of ·OH in 4T1 tumor cells. First, 2',7'-dichlorofluorescein diacetate (DCFH-DA) was used to detect the ROS in cells. When DCFH-DA freely passes through cell membrane, intracellular esterase will hydrolyze it to produce DCFH without fluorescence, which then is oxidized by intracellular ROS to form DCF with green fluorescence. As expected, Au@Cu_{2-x}Se + H₂O₂ group exhibited a green fluorescence in CLSM images, whereas Au@Cu_{2-x}Se + H₂O₂ + NIR group showed the strongest green fluorescence (Additional file 1: Fig. S12), manifesting that Au@Cu_{2-x}Se NPs and NIR could collaboratively enhance the ROS content in tumor cells. Next, mitochondrial hydroxyl radical detection assay kit was used to specifically detect the generation of ·OH radicals at cell level. The cell-permeable OH580 probe can selectively react with ·OH present in live cells to generate a red fluorescence signal. As shown in Fig. 3C, Au@Cu_{2-x}Se + H₂O₂ + NIR group showed a significantly higher fluorescence signal than other groups, further confirming that photothermal can accelerate the Fenton-like reaction catalyzed by Au@Cu_{2-x}Se NPs to produce abundant ·OH radicals in tumor cells.

The biocompatibility of nanoagent is another important criterion for biomedical applications. Cytotoxicity of Au@Cu_{2-x}Se NPs on HEK293 normal cells and 4T1 tumor cells was then investigated. Various concentrations of Au@Cu_{2-x}Se NPs were incubated with cells for 24 h. Then the cell viability was monitored by Cell Counting Kit-8 (CCK-8) assay. Negligible cytotoxicity to both normal cells (Additional file 1: Fig. S13) and tumor cells (Fig. 4A) were observed after incubation with Au@Cu_{2-x}Se NPs at low concentration ($\leq 100 \mu\text{g mL}^{-1}$). Interestingly, when the concentration of Au@Cu_{2-x}Se NPs was below $50 \mu\text{g mL}^{-1}$, the cell viability of 4T1 tumor cells was higher than that of control group ($0 \mu\text{g mL}^{-1}$). According to previous reports, ROS with a proper concentration is a messenger to mediate the normal physiological process, while excess ROS can destroy the antioxidant system of cell and induce cell death [1–3]. Noting that there are trace amounts of H₂O₂ in tumor cell, small amount of ·OH will be generated through Fenton-like reaction after introducing Au@Cu_{2-x}Se with low concentration. So, the trace ·OH as a messenger might promote cell growth [1, 2]. When the concentration of Au@Cu_{2-x}Se reached $200 \mu\text{g mL}^{-1}$, cell viability began to

decline. These results suggest good biocompatibility of Au@Cu_{2-x}Se at low concentration.

The cellular uptake ability of Au@Cu_{2-x}Se NPs was also examined. After incubated with Au@Cu_{2-x}Se NPs for various times, the content of Au in 4T1 tumor cells was quantified by inductively coupled plasma mass spectrometry (ICP-MS). Additional file 1: Fig. S14 presents that Au@Cu_{2-x}Se NPs could be effectively internalized by tumor cells, and the amount of ingestion increased with increasing incubation time.

A relatively low concentration ($50 \mu\text{g mL}^{-1}$) was chosen to investigate the in vitro anti-proliferation effect of Au@Cu_{2-x}Se NPs via PTT + CDT (Fig. 4B). Incubation of 4T1 tumor cells with Au@Cu_{2-x}Se, H₂O₂, or NIR alone showed negligible influence on cell viability. When cells were treated with either Au@Cu_{2-x}Se + NIR or Au@Cu_{2-x}Se + H₂O₂, substantial decrease in cell viability was observed. Especially, cells treated with Au@Cu_{2-x}Se + H₂O₂ + NIR exhibited much more apparent decline in cell viability, showing the synergistically enhanced antitumor effect. CLSM was then employed to visualize the cell killing induced by hyperthermia and ·OH. Cells cultured under different conditions were co-stained with Calcein AM (living cells staining, green fluorescence) and PI (dying cells staining, red fluorescence). The CLSM images (Additional file 1: Fig. S15) revealed that a portion of 4T1 tumor cells was killed cultured under the condition of either Au@Cu_{2-x}Se + H₂O₂ or Au@Cu_{2-x}Se + NIR. Reasonably, when cells were treated with Au@Cu_{2-x}Se + H₂O₂ + NIR, almost all cells were dead. Subsequently, an Annexin V-FITC/PI method was carried out by flow cytometry to characterize cell apoptosis and necrosis after different treatments. Figure 4C presents that cells treated with Au@Cu_{2-x}Se + H₂O₂ + NIR showed the most obvious late apoptosis or necrosis than cells treated with other treatments. Moreover, immunofluorescent staining of γ -H2AX found that Au@Cu_{2-x}Se + H₂O₂ treatment induced the formation of apoptotic ring (Fig. 4D). According to previous report, nuclear γ -H2AX apoptotic ring, which can be detected in early apoptotic cells, is usually caused by early DNA breaks at the nuclear periphery [26]. So we speculate that the ·OH generated outside the nucleus attacks DNA at the nuclear periphery and initiates cell apoptosis. Of course, Au@Cu_{2-x}Se + H₂O₂ + NIR treatment caused more serious DNA damage.

In vivo biosafety of Au@Cu_{2-x}Se NPs

It is necessary to test the biosafety of Au@Cu_{2-x}Se NPs before in vivo application. Hemolysis assay was firstly

(See figure on next page.)

Fig. 4 **A** Cytotoxicity of Au@Cu_{2-x}Se NPs toward 4T1 tumor cells at different concentrations. **B** 4T1 tumor cell viability after different treatments. Data are presented as mean \pm s.d. (n = 6). *P < 0.05, **P < 0.01, ***P < 0.001. **C** Flow cytometric analysis of 4T1 tumor cells after different treatments. **D** CLSM images of 4T1 tumor cells after different treatments, where DAPI (blue) and γ -H2AX (red) were used to observe the cell nucleus and DAN damage, respectively. Scale bar = 20 μm . Au@Cu_{2-x}Se: $50 \mu\text{g mL}^{-1}$. H₂O₂: $100 \mu\text{M}$. NIR: 808 nm laser, 1.0 W cm^{-2} for 5 min

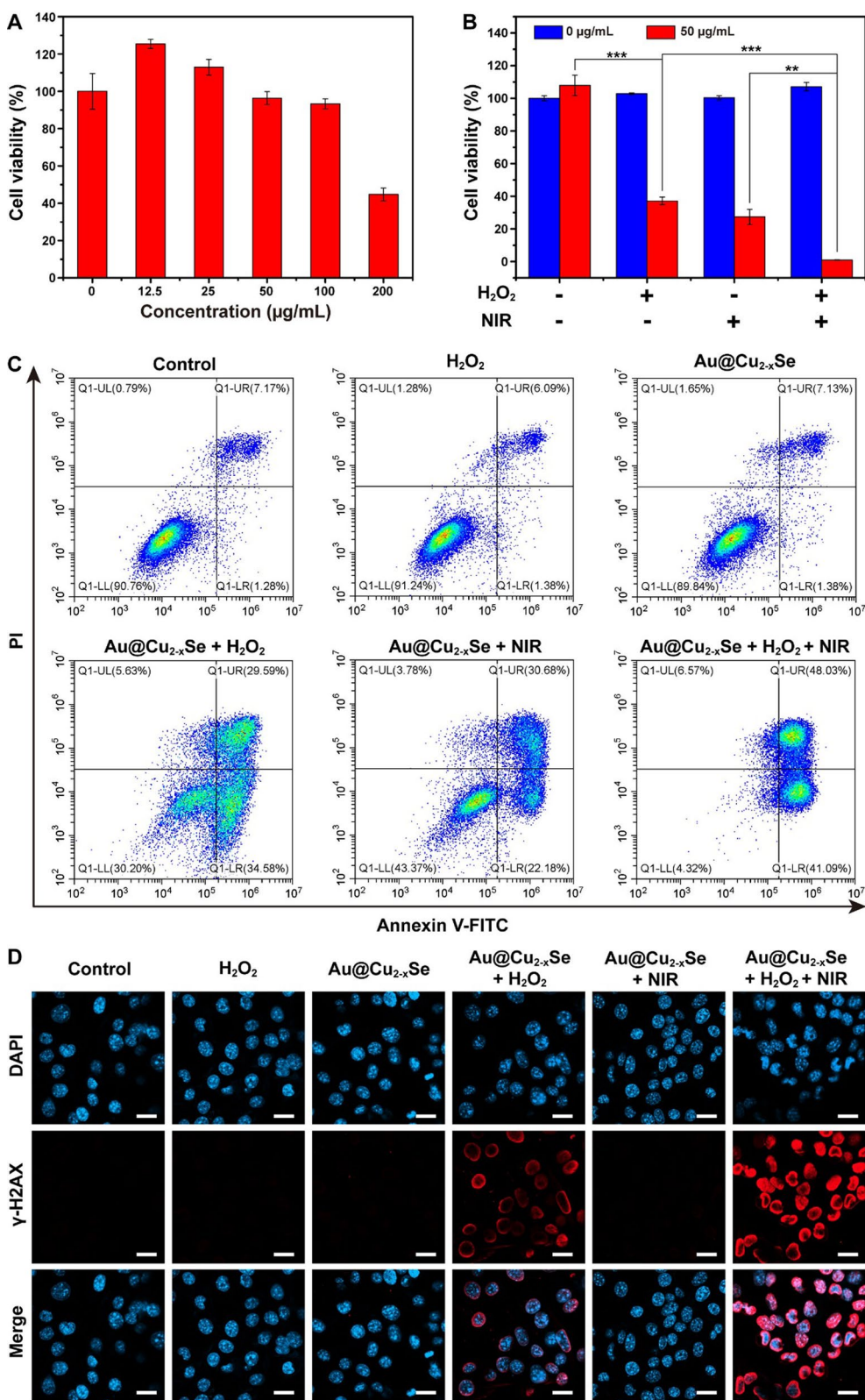


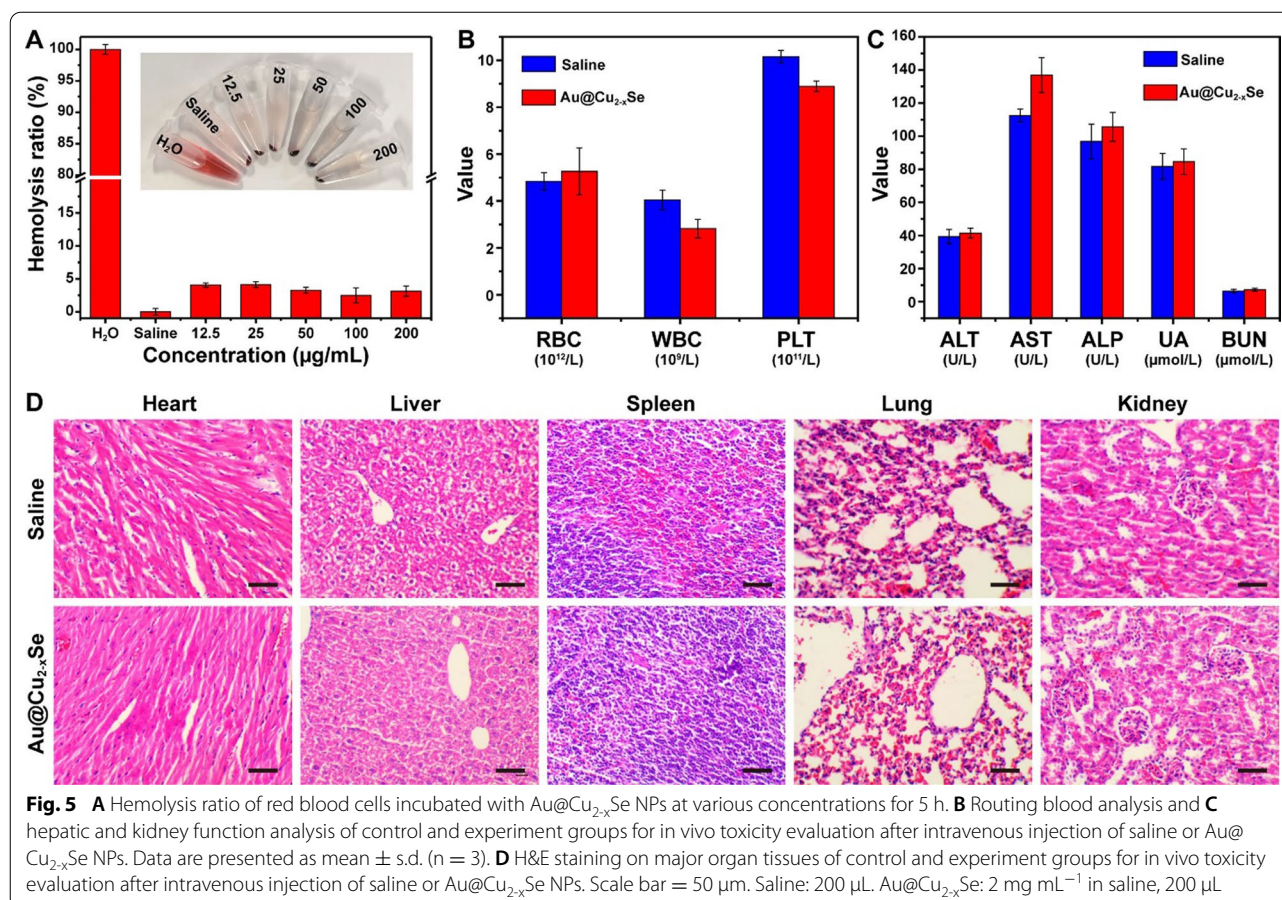
Fig. 4 (See legend on previous page.)

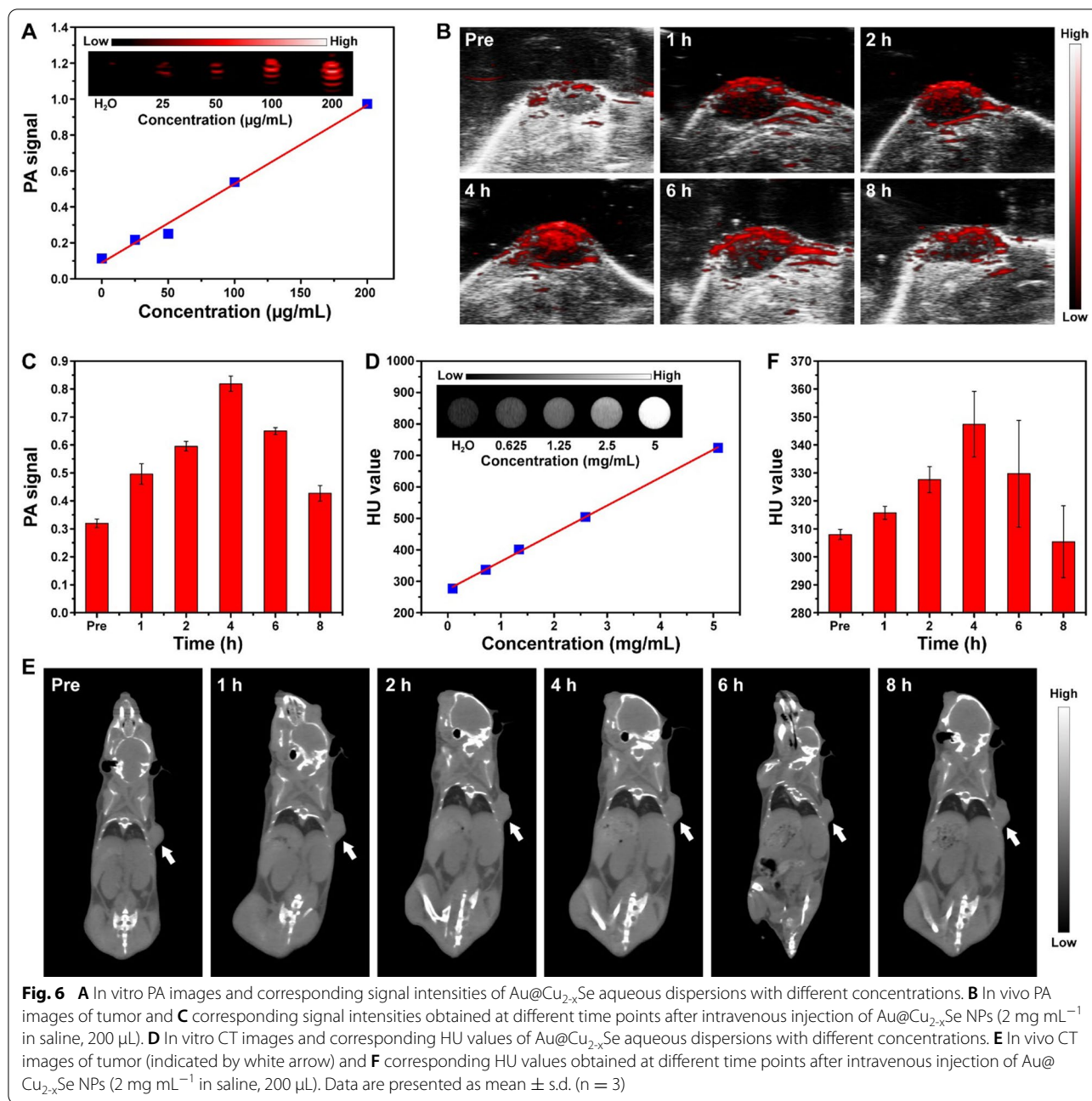
conducted to investigate the influence of Au@Cu_{2-x}Se NPs on hemolysis of red blood cells, using pure water and saline as positive and negative controls, respectively. The calculated hemolysis ratios were less than 5% at all concentrations (Fig. 5A), indicating the acceptable blood compatibility of Au@Cu_{2-x}Se NPs. After saline (control group) and Au@Cu_{2-x}Se suspended in saline (2 mg mL⁻¹, 200 μL) were injected into mice via intravenous injection, mice were observed for 14 days. The mice in Au@Cu_{2-x}Se NPs group revealed no evident weight decrease, confirming the low systemic toxicity of Au@Cu_{2-x}Se NPs (Additional file 1: Fig. S16). To determine the long-term toxicity of Au@Cu_{2-x}Se NPs, hematological biochemistry indexes were analyzed at 14 d. The changes of routine blood parameters, including red blood cells (RBC), white blood cells (WBC), platelets (PLT), were within acceptable ranges (Fig. 5B). Hepatic and kidney function indexes, including alanine aminotransferase (ALT), aspartate aminotransferase (AST), alkaline phosphatase (ALP), uric acid (UA), and blood urea nitrogen (BUN), fell into normal range (Fig. 5C). Hematoxylin and eosin (H&E) staining analyses on major organ tissues (i.e., heart, liver, spleen, lung, and kidney) were also conducted.

H&E results revealed no observable tissue damage or inflammatory lesions (Fig. 5D). Taken together, such experiments confirm that Au@Cu_{2-x}Se NPs provided insignificant systemic toxicity under the treatment dose, strengthening their biomedical utilization as a safe therapeutic nanoagent.

In vitro and in vivo PA/CT imaging of Au@Cu_{2-x}Se NPs

The high photothermal conversion efficiency means that Au@Cu_{2-x}Se NPs could be a contrast agent for PA imaging. The PA imaging performance of Au@Cu_{2-x}Se NPs was then evaluated on an ultrasound-photoacoustic dual-mode imaging system, wherein the excitation wavelength for PA was 808 nm. Figure 6A presents that the in vitro PA signal increased linearly with the increase of concentration of Au@Cu_{2-x}Se NPs. After saline containing Au@Cu_{2-x}Se NPs (2 mg mL⁻¹, 200 μL) was intravenously injected into 4T1 tumor-bearing mice, the PA signal (labeled with red) in the tumor region (localized by ultrasonic signal labeled with gray) was gradually enhanced to the maximum at around 4 h post-injection (Fig. 6B, C), which might be ascribed to the enhanced permeability and retention (EPR) effect of NPs in tumor. The maximal





PA signal was 2.6 times higher than that acquired before the injection of Au@Cu_{2-x}Se NPs (Fig. 6 C). The time-dependent PA image indicates that Au@Cu_{2-x}Se NPs reached the maximum accumulation in tumor at 4 h after intravenous injection.

Au is a high-Z element and has the capability of X-ray attenuation. So the CT imaging performance of Au@Cu_{2-x}Se NPs was also assessed. The imaging brightness and Hounsfield unit (HU) values of Au@Cu_{2-x}Se aqueous dispersions increased with the increasing NPs concentration

(Fig. 6D). After saline containing Au@Cu_{2-x}Se NPs (2 mg mL⁻¹, 200 µL) was administrated into tumor-bearing mice intravenously, the HU value at tumor site increased from 308.0 before injection to 347.4 after 4 h injection (Fig. 6E, F). When changing the injection method from intravenous injection to intratumoral injection, a strong whitening effect was observed (Additional file 1: Fig. S17). These results make us believe that Au@Cu_{2-x}Se NPs have the potential to be a contrast-enhancing agent for CT imaging.

In vivo photothermal and chemodynamic therapy based on Au@Cu_{2-x}Se NPs

Inspired by the in vitro anticancer effects, the in vivo therapeutic effect of PTT + CDT based on Au@Cu_{2-x}Se NPs was examined by establishing 4T1 tumor-bearing mice. Tumor-bearing mice were divided randomly into five groups: (1) saline; (2) saline + NIR (1.5 W cm⁻²); (3) Au@Cu_{2-x}Se; (4) Au@Cu_{2-x}Se + NIR (1.0 W cm⁻²); (5) Au@Cu_{2-x}Se + NIR (1.5 W cm⁻²). The NIR irradiation was administrated at 4 h after intravenous injection of Au@Cu_{2-x}Se NPs suspended in saline, since PA and CT imaging showed maximal accumulation of Au@Cu_{2-x}Se NPs in tumor at this time point. The tumor temperature in Au@Cu_{2-x}Se + NIR (1.5 W cm⁻²) group rapidly increased from 31.5 to 48.9 °C in 5 min of 808 nm NIR irradiation at the power density of 1.5 W cm⁻², which was higher than that in saline + NIR (1.5 W cm⁻²) group under the same NIR power density (Fig. 7A, B). These validate the effective intratumoral accumulation of Au@Cu_{2-x}Se NPs and their excellent in vivo photothermal conversion performance. During the therapeutic period, all mice in each group displayed no apparent decrease in body weight (Fig. 7C), H&E staining on major organs from all groups showed no obvious damages (Additional file 1: Fig. S18), implying the negligible adverse effects of these treatments on mice. As for the suppressing performance toward tumor growth, Au@Cu_{2-x}Se + NIR (1.5 W cm⁻²) treatment was much more effective than other treatments (Fig. 7D, E and Additional file 1: Fig. S19), ascribing to the synergistic enhancement of PTT and boosted CDT.

To confirm the in vivo photothermal enhanced CDT effect, tumors in saline + NIR (1.5 W cm⁻²) group were irradiated with NIR at 1.5 W cm⁻², while tumors in Au@Cu_{2-x}Se + NIR (1.0 W cm⁻²) group were irradiated with NIR at 1.0 W cm⁻². The tumor temperature in Au@Cu_{2-x}Se + NIR (1.0 W cm⁻²) group increased from 32.7 to 40.5 °C in 5 min of NIR irradiation (Fig. 7A, B). A similar tumor temperature increase was also observed in saline + NIR (1.5 W cm⁻²) group (Fig. 7A, B). So these treatments could ensure that the temperature conditions at tumor sites in these two groups were close to each other. The inhibition efficiency of tumor growth in Au@Cu_{2-x}Se + NIR (1.0 W cm⁻²) group was higher than that of both Au@Cu_{2-x}Se group and saline + NIR (1.5 W cm⁻²) group (Fig. 7D, E). Considering that the tumor temperature in Au@Cu_{2-x}Se + NIR (1.0 W cm⁻²) group was higher than that in Au@Cu_{2-x}Se group and was close to that in saline + NIR (1.5 W

cm⁻²) group, the anti-tumor effect of Au@Cu_{2-x}Se + NIR (1.0 W cm⁻²) could be attributed to the photothermal enhanced CDT effect. However, tumors in Au@Cu_{2-x}Se + NIR (1.0 W cm⁻²) group were inhibited, but were not eliminated, suggesting that the insufficient ·OH and mild photothermal produced in this group were not able to completely destroy the tumor. When the NIR power density was increased to 1.5 W cm⁻², that was, Au@Cu_{2-x}Se + NIR (1.5 W cm⁻²) group, the tumors could be completely suppressed in the first eight days, substantiating the synergistic enhancement of PTT and boosted CDT in vivo.

The tumors from the representative mouse in each group after NIR irradiation were collected to verify the generation of ROS by using DCFH-DA as ROS probe. As presented in Fig. 7F, unlike saline group and saline + NIR group, both of which showed undetectable green fluorescence corresponding to ROS, Au@Cu_{2-x}Se group exhibits a weak green fluorescence, while Au@Cu_{2-x}Se + NIR (1.0 W cm⁻²) group and Au@Cu_{2-x}Se + NIR (1.5 W cm⁻²) group displayed an obvious enhanced green fluorescence. These results may be attributed to the fact that the intratumorally accumulated Au@Cu_{2-x}Se NPs could induce the generation of ROS in tumor through photothermal-assisted Fenton-like reaction [27].

It should be noted that the tumor growth in Au@Cu_{2-x}Se group was not suppressed after single CDT treatment (Fig. 7D). The reason for this phenomenon may be that the in vivo Fenton-like kinetics catalyzed by Au@Cu_{2-x}Se only are not fast enough without the assistance of exogenous energy, so that the cell damage caused by in situ generated ·OH could be repaired by the oxidative damage repair system in the first few days after CDT treatment. To prove this supposition, H&E staining, as well as terminal deoxynucleotidyl transferase-mediated dUTP nick-end labeling (TUNEL) staining of tumor tissues, were performed to detect cell damage after different therapies. To avoid the complete repair of oxidative damage, the tumor from the representative mouse in each group at 20 h post-treatment was collected. As shown in Fig. 7 E, a slight portion of necrosis and apoptosis was observed in Au@Cu_{2-x}Se group compared with that in saline group, implying that single CDT treatment might cause cell damage in the early stage. The extent and severity of necrosis and apoptosis in Au@Cu_{2-x}Se + NIR (1.0 W cm⁻²) group were higher than those in both Au@Cu_{2-x}Se group and saline + NIR (1.5 W cm⁻²) group, validating the photothermal enhanced CDT effect.

(See figure on next page.)

Fig. 7 **A** Thermal images and **B** temperature rise curves at tumor sites of 4T1 tumor-bearing mice after intravenous injection of saline or Au@Cu_{2-x}Se NPs followed by NIR irradiation. **C** Body weight changes, **D** tumor volume growth curves, and **E** digital photographs of 4T1 tumor-bearing mice after intravenous injection of saline or Au@Cu_{2-x}Se NPs followed by NIR irradiation. Data are presented as mean ± s.d. (n = 5). *P < 0.05, **P < 0.01, ***P < 0.001. **F** DCFH-DA, H&E, and TUNEL staining of tumor tissues after corresponding treatments, where blue represents the cell nucleus stained with DAPI. Scale bar = 50 μm. Saline: 200 μL. Au@Cu_{2-x}Se: 2 mg mL⁻¹ in saline, 200 μL. NIR: 808 nm laser, 1.0 or 1.5 W cm⁻² for 5 min

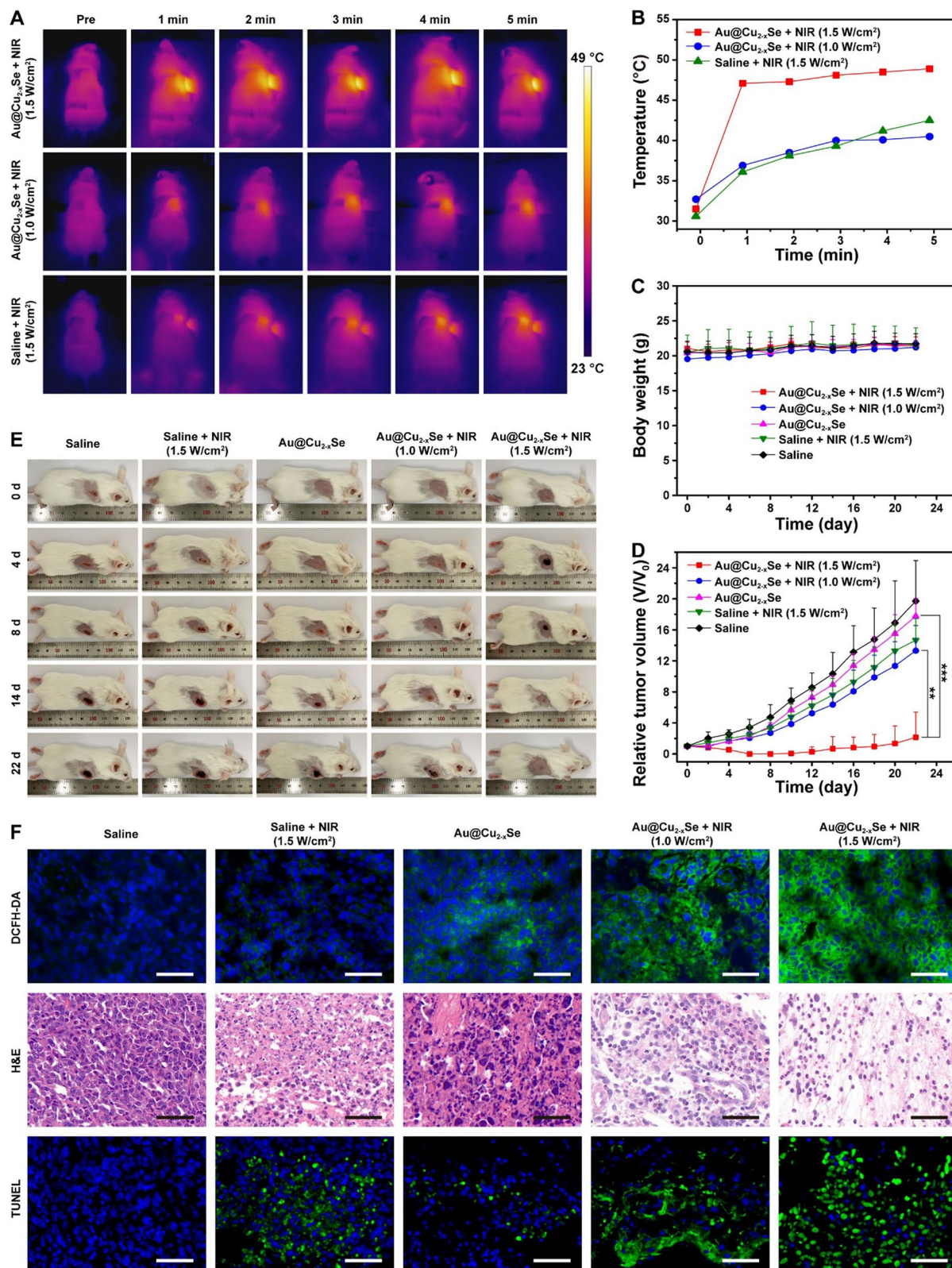


Fig. 7 (See legend on previous page.)

Of course, the Au@Cu_{2-x}Se NPs + NIR (1.5 W cm⁻²) group had the most severe cell death.

Intratumoral injection of Au@Cu_{2-x}Se NPs was also conducted to evaluate the in vivo synergistic therapy of PTT + CDT. The tumor temperature in Au@Cu_{2-x}Se + NIR group rapidly increased from 33.1 to 57.7 °C in 5 min of 808 nm NIR irradiation at 0.5 W cm⁻², while no obvious temperature increase was observed in saline + NIR group under the same NIR condition (Additional file 1: Fig. S20). During the therapeutic period, all mice in each group displayed no apparent decrease in body weight (Additional file 1: Fig. S21A). As for the suppressing performance toward tumor growth, Au@Cu_{2-x}Se + NIR treatment was much more effective than other treatments, and the tumors in this group were completely eradicated after 16 days (Additional file 1: Fig. S21B, C). H&E and TUNEL staining on tumors collected at 20 h post-treatment revealed considerably increased necrosis and apoptosis of tumor cells in Au@Cu_{2-x}Se + NIR group (Additional file 1: Fig. S22).

Conclusions

In summary, we have exploited the application of core-shell Au@Cu_{2-x}Se NPs acting as a theranostic nanoagent for PA/CT imaging-mediating synergistic therapy of PTT + CDT in the field of cancer treatment. The Au@Cu_{2-x}Se NPs were fabricated through a facile two-step reduction method. Biosafety study certificated the qualification of Au@Cu_{2-x}Se NPs in biocompatibility. Imaging assessment indicated that Au@Cu_{2-x}Se NPs could be a contrast agent for PA and CT imaging. In vitro and in vivo examinations revealed that the high photothermal conversion efficiency of Au@Cu_{2-x}Se NPs not only permits the PTT efficacy but also facilitates the CDT effect assisted by the heat generated in PTT process, thus clarifying a combinational therapeutic PTT + CDT outcome for the inhibition of tumor growth. This versatile agent may provide a paradigm to realize an accurate and noninvasive theranostic approach for cancer treatment.

Experimental section

Materials

Hydrogen Tetrachloroaurate(III) Trihydrate (HAuCl₄·3H₂O) and methylene blue (MB) were obtained from Shanghai Titan Technology Co., Ltd. Copper(II) sulfate pentahydrate (CuSO₄·5H₂O), selenium dioxide (SeO₂), sodium citrate dihydrate, ascorbic acid, and hydrogen peroxide (H₂O₂) were purchased from Sinopharm Chemical Reagent Co., Ltd. Polyvinylpyrrolidone (PVP, Mw ~55,000), 2',7'-dichlorofluorescein diacetate (DCFH-DA), and Calcein AM were provided by Sigma Aldrich. Roswell Park Memorial Institute 1640 (RPMI-1640) was supported by Corning Incorporated. Fetal

bovine serum (FBS), trypsin, and penicillin-streptomycin solution were supplied from Gibco Company. Cell Counting Kit-8 (CCK-8) solution was purchased from Dojindo Laboratories. Hoechst 33,342, 4',6-diamidino-2-phenylindole (DAPI), and propidium iodide (PI) were acquired from Beyotime Biotechnology. Mitochondrial hydroxyl radical detection assay, anti-gamma H2AX (phospho S139) antibody [EP854(2)Y], and goat polyclonal secondary antibody to rabbit IgG - H&L (Alexa Fluor® 647) were purchased from Abcam Company. Accutase™ Cell Detachment Solution and FITC Annexin V Apoptosis Detection Kit were supplied from BD Bioscience. All chemicals and reagents were used as received without further purification.

Synthesis of Au NPs

HAuCl₄ aqueous solution prepared by mixing 1.215 mL of 10 mM HAuCl₄ solution and 50 mL of deionized water was heated to slight boiling. A condenser was utilized to prevent the evaporation of the water. Then 50 mL of 10 mg mL⁻¹ sodium citrate solution was added into the boiling HAuCl₄ solution. After keeping boiling for 15 min under continuous stirring, the mixture was allowed to cool to room temperature. The resulted Au NPs were collected by centrifuging the suspension at 15,000 rpm for 15 min.

Synthesis of Au@Cu_{2-x}Se NPs

5.5 mL of Au NPs redispersed in deionized water was mixed with 1.6 mL of 10 mg mL⁻¹ PVP solution and kept stirring at 30 °C for 1 h, followed by the addition of 0.1 mL of 0.1 M SeO₂ and 0.3 mL of 0.2 M ascorbic acid solution. After reaction for 30 min, a mixed solution of 0.1 mL of 0.2 M CuSO₄ and 0.4 mL of 0.2 M ascorbic acid was added. After stirring the suspension at 30 °C for another 10 h, the Au@Cu_{2-x}Se NPs were collected by centrifuging the suspension at 15,000 rpm for 15 min and washed three times with deionized water.

Synthesis of Cu_{2-x}Se NPs

1.6 mL of 10 mg mL⁻¹ PVP solution was added into 5.5 mL of deionized water and kept stirring at 30 °C, followed by the addition of 0.1 mL of 0.1 M SeO₂ and 0.3 mL of 0.2 M ascorbic acid solution. After reaction for 30 min, a mixed solution of 0.1 mL of 0.2 M CuSO₄ and 0.4 mL of 0.2 M ascorbic acid was added. After stirring the suspension at 30 °C for another 10 h, the Cu_{2-x}Se NPs were collected by centrifuging the suspension at 15,000 rpm for 15 min and washed three times with deionized water.

Characterization

The morphology and structure were characterized by transmission electron microscopy (TEM, JEOL

JEM-2100 F). The crystal structure was determined by X-ray diffraction (XRD, Rigaku D/max2500). The chemical state was analyzed by X-ray photoelectron spectroscopy (XPS, Thermo Escalab 250), and the binding energy of C 1 s peak at 284.8 eV was taken as an internal standard. Fourier transform infrared (FTIR) spectrum was recorded on Bruker Tensor-27 spectrometer. Ultraviolet-visible-infrared (UV-vis-NIR) absorption spectrum was scanned on Persee TU-1901 spectrometer. The metal element content was determined by inductively coupled plasma optical emission spectroscopy (ICP-OES, Varian 710ES). Hydrodynamic size and zeta potential were characterized by a particle size zeta potential analyzer (Malvern ZEN3690).

Photothermal performance

An 808 NIR laser was used to estimate the photothermal performance of Au@Cu_{2-x}Se NPs. The NIR power density was maintained at 1.0 W cm⁻² in all tests. The volume of Au@Cu_{2-x}Se aqueous dispersions in each test was 1.5 mL. Temperature changes were recorded by a thermal camera. For concentration-dependent photothermal performance, various Au@Cu_{2-x}Se aqueous dispersions in a quartz cuvette with concentrations of 0, 25, 50, 100, and 200 µg mL⁻¹ were exposed to laser for 10 min. To evaluate the photothermal stability, Au@Cu_{2-x}Se aqueous dispersion with a concentration of 50 µg mL⁻¹ was irradiated by laser for 10 min (laser on) followed by natural cooling without irradiation for another 10 min (laser off). Such heating/cooling processes were repeated 6 times. Heating-cooling curve was obtained by continuously irradiating 50 µg mL⁻¹ dispersion with laser for 15 min, and then turning off the laser to allow the dispersion to naturally cool to room temperature. Following previously reported method [8, 20, 28], the photothermal conversion efficiency was calculated according to Eqs. 1–4.

$$\eta = \frac{hS(T_{\max} - T_{\max, H_2O})}{I(1 - 10^{-A_\lambda})} \quad (1)$$

$$hS = \frac{mC_p}{\tau_s} \quad (2)$$

$$t = -\tau_s \ln \theta \quad (3)$$

$$\theta = \frac{T - T_{\text{sur}}}{T_{\max} - T_{\text{sur}}} \quad (4)$$

where η is the photothermal conversion efficiency, h is the heat-transfer coefficient, S is the surface area of container, T is the temperature of Au@Cu_{2-x}Se aqueous dispersion, T_{\max} is the maximum temperature of Au@Cu_{2-x}Se aqueous dispersion, T_{\max, H_2O} is the maximum

temperature of pure water, T_{sur} is the ambient temperature of surroundings, I is the laser power, A_λ is the absorbance of Au@Cu_{2-x}Se aqueous dispersion at the wavelength of 808 nm, m and C_p are the mass (1.5 g) and heat capacity (4.2 J g⁻¹) of solvent (water), t is the cooling time, τ_s is the time constant of sample system, θ is the driving force temperature. τ_s can be obtained by applying the linear time data from the cooling period vs. $-\ln \theta$ (Fig. 2D, E).

Photothermal enhanced Fenton-like catalytic performance

An MB degradation assay was used to monitor the ·OH generation. First, mixed aqueous solutions of Au@Cu_{2-x}Se and MB remained static state in the dark for 30 min at 25, 37, and 42 °C, respectively. Second, after adding H₂O₂, the mixtures were then remained static state in the dark for another 30 min at 25, 37, or 42 °C, respectively. The final concentrations of Au@Cu_{2-x}Se NPs, MB, and H₂O₂ in mixtures were set at 100 µg mL⁻¹, 10 µg mL⁻¹, and 10 mM, respectively. Finally, after removing Au@Cu_{2-x}Se NPs via centrifugation at 15,000 rpm for 15 min, the absorbance of each supernatant at 664 nm was measured. In these experiments, the pure MB solution (10 µg mL⁻¹), and the mixture of MB (10 µg mL⁻¹) and H₂O₂ (10 mM) solution, were chosen as control.

Next, ESR was used to confirm the generation of ·OH in Fenton-like reaction. DMPO was used as a spin trap agent for ·OH. After keeping the mixed aqueous solutions of Au@Cu_{2-x}Se, H₂O₂, and DMPO for 5 min at 25, 37, and 42 °C, the mixtures were used to record ESR spectra by a spectrometer (Bruker ELEXSYS E500, CW X-band), respectively. The final concentrations of Au@Cu_{2-x}Se, H₂O₂, and DMPO were set at 50 µg mL⁻¹, 100 µM, and 50 mM, respectively. The mixture of Au@Cu_{2-x}Se (50 µg mL⁻¹) and DMPO (50 mM), and the mixture of H₂O₂ (100 µM) and DMPO (50 mM), were chosen as control.

To prove the photothermal accelerated ·OH generation in Fenton-like reaction, 1.5 mL of mixed aqueous solution of Au@Cu_{2-x}Se NPs, MB, and H₂O₂ was irradiated with or without 808 nm NIR laser at 1.0 W cm⁻² for 10 min. The final concentrations of Au@Cu_{2-x}Se NPs, MB, and H₂O₂ in mixture were set at 100 µg mL⁻¹, 10 µg mL⁻¹, and 10 mM, respectively. The Temperature rise was recorded by thermal camera. Finally, after removing Au@Cu_{2-x}Se NPs via centrifugation at 15,000 rpm for 15 min, the absorbance of supernatant at 664 nm was measured.

Detection of intracellular ROS

CLSM (Zesis LSM800) was adopted to detect the intracellular ROS by using DCFH-DA (Sigma-Aldrich) as ROS probe. Cells were divided into six groups, including

(1) control, (2) H_2O_2 , (3) $\text{Au@Cu}_{2-x}\text{Se}$, (4) $\text{Au@Cu}_{2-x}\text{Se} + \text{H}_2\text{O}_2$, (5) $\text{Au@Cu}_{2-x}\text{Se} + \text{NIR}$, and (6) $\text{Au@Cu}_{2-x}\text{Se} + \text{H}_2\text{O}_2 + \text{NIR}$. First, 2×10^5 4T1 tumor cells were seeded into the CLSM-specific culture disk and then cultured at 37°C under 5% CO_2 for 24 h. Second, after replacing the culture medium with 1 mL of FBS-free RPMI-1640 medium containing $\text{Au@Cu}_{2-x}\text{Se}$ ($50 \mu\text{g mL}^{-1}$) or H_2O_2 ($100 \mu\text{M}$), the cells in group (5) and (6) were irradiated with NIR laser (1.0 W cm^{-2}) for 5 min, respectively. After irradiation, the cells continued to incubate for 30 min. Third, after washing the cells three times with PBS, the cells were incubated with 1 mL of FBS-free RPMI-1640 medium containing DCFH-DA ($10 \mu\text{M}$) and Hoechst 33,342 ($5 \mu\text{g mL}^{-1}$) for 20 min. Fourth, the cells were washed three times with PBS followed by the addition of 1 mL of FBS-free RPMI-1640 medium. Then the fluorescence images of cells were collected by CLSM.

Detection of intracellular $\cdot\text{OH}$ radicals

Mitochondrial hydroxyl radical detection assay kit (Abcam) was used to detect the intracellular $\cdot\text{OH}$. First, 2×10^5 4T1 tumor cells were seeded into the CLSM-specific culture disk and then cultured for 24 h. Second, after replacing the culture medium with 200 μL of the prepared OH580 stain working solution, the cells continued to incubate for 1 h without light. Third, after washing the cells one time with PBS, the cells were incubated with 1 mL of RPMI-1640 complete medium containing $\text{Au@Cu}_{2-x}\text{Se}$ ($50 \mu\text{g mL}^{-1}$) or H_2O_2 ($100 \mu\text{M}$), and then irradiated with or without NIR laser (1.0 W cm^{-2}) for 5 min. After irradiation, the cells continued to incubate for 30 min. Fourth, the cells were incubated with 1 mL of PBS containing Hoechst 33,342 ($5 \mu\text{g mL}^{-1}$) for 10 min. Fifth, the cells were washed three times with PBS followed by the addition of 1 mL assay buffer. Then the fluorescence images of cells were collected by CLSM.

In vitro cytotoxicity assay

The cytotoxicity of $\text{Au@Cu}_{2-x}\text{Se}$ against HEK293 normal cells and 4T1 tumor cells were examined via a CCK-8 assay. HEK293 normal cells or 4T1 tumor cells were seeded into 96-well plate at 1×10^4 cells/well and incubated for 24 h. Then the cells were incubated in 100 μL of the complete medium containing $\text{Au@Cu}_{2-x}\text{Se}$ NPs at various concentrations of 0, 12.5, 25, 50, 100, and 200 $\mu\text{g mL}^{-1}$. After 24 h, the culture medium was removed and the cells were washed three times with PBS. Then the cells were incubated in 100 μL of complete medium containing 10 μL CCK-8. After another 1–2 h, the optical densities of each well were recorded at 450 nm on a microplate reader (BioTek Cytation 3).

In vitro cellular uptake

First, 4T1 tumor cells were seeded into 6-well plate at 1.5×10^5 cells/well and then cultured at 37°C under 5% CO_2 for 24 h. Second, after replacing the culture medium with 1 mL of the complete medium containing $\text{Au@Cu}_{2-x}\text{Se}$ NPs ($50 \mu\text{g mL}^{-1}$), the cells were then incubated for 0.5, 1, 2, 4, and 8 h, respectively (three wells at each time point). Third, the culture medium was removed and the cells were washed three times with PBS, digested with 0.25% trypsin (Gibco), and centrifuged at 1500 rpm for 3 min. When the collected cells were redispersed in 1 mL PBS, the cells were counted. Finally, the content of Au in PBS was analyzed by ICP-MS.

In vitro PTT and CDT

4T1 tumor cells were divided into eight groups, including (1) control, (2) H_2O_2 , (3) NIR, (4) $\text{H}_2\text{O}_2 + \text{NIR}$, (5) $\text{Au@Cu}_{2-x}\text{Se}$, (6) $\text{Au@Cu}_{2-x}\text{Se} + \text{H}_2\text{O}_2$, (7) $\text{Au@Cu}_{2-x}\text{Se} + \text{NIR}$, and (8) $\text{Au@Cu}_{2-x}\text{Se} + \text{H}_2\text{O}_2 + \text{NIR}$. First, 4T1 tumor cells were seeded into 96-well plate at 1×10^4 cells/well and incubated for 24 h. Second, after replacing the culture medium with 100 μL of the complete medium containing $\text{Au@Cu}_{2-x}\text{Se}$ ($50 \mu\text{g mL}^{-1}$) or H_2O_2 ($100 \mu\text{M}$), the cells were irradiated with or without NIR laser (1.0 W cm^{-2}) for 5 min. After irradiation, the cells continued to incubate for 24 h. Third, the culture medium was removed and the cells were washed three times with PBS. Then the cells were incubated in 100 μL of complete medium containing 10 μL CCK-8 for another 1 h. Finally, the optical densities of each well were recorded at 450 nm on a microplate reader.

CLSM was then employed to observe the cell death induced by hyperthermia and $\cdot\text{OH}$ radicals. First, 2×10^5 4T1 tumor cells were seeded into the CLSM-specific culture disk and then cultured at 37°C under 5% CO_2 for 24 h. Second, after replacing the culture medium with 1 mL of the complete medium containing $\text{Au@Cu}_{2-x}\text{Se}$ ($50 \mu\text{g mL}^{-1}$) or H_2O_2 ($100 \mu\text{M}$), the cells were irradiated with or without NIR laser (1.0 W cm^{-2}) for 5 min. After irradiation, the cells continued to incubate for 4 h. Third, the culture medium was replaced by 1 mL of PBS containing Calcein AM ($2 \mu\text{M}$) and PI ($4 \mu\text{M}$) and co-incubated with the cells for another 20 min. Finally, the fluorescence images of cells were collected directly by CLSM.

In vitro apoptosis and necrosis analysis by flow cytometry

First, 4T1 tumor cells were seeded into 12-well plate at 7×10^4 cells/well and then cultured at 37°C under 5% CO_2 for 24 h. Second, after replacing the culture medium with 1 mL of the complete medium containing $\text{Au@Cu}_{2-x}\text{Se}$ ($50 \mu\text{g mL}^{-1}$) or H_2O_2 ($100 \mu\text{M}$), the cells were

irradiated with or without NIR laser (1.0 W cm^{-2}) for 5 min. After irradiation, the cells continued to incubate for 24 h. Third, the cells were digested with Accutase™ Cell Detachment Solution (BD Biosciences) and re-suspended in PBS. Then, the cells were stained according to the FITC Annexin V Apoptosis Detection Kit (BD Biosciences) and quantified by flow cytometry (Beckman Cytoflex).

In vitro DNA damage analysis

First, 2×10^5 4T1 tumor cells were seeded into the CLSM-specific culture disk and then cultured for 24 h. Second, after replacing the culture medium with 1 mL of RPMI-1640 complete medium containing Au@Cu_{2-x}Se ($50 \mu\text{g mL}^{-1}$) or H₂O₂ ($100 \mu\text{M}$), the cells were irradiated with or without NIR laser (1.0 W cm^{-2}) for 5 min. After irradiation, the cells continued to incubate for 6 h. Third, these cells were fixed with 4% paraformaldehyde for 10 min, washed several times with PBS, permeabilized with immunostaining permeabilization buffer with triton X-100 (Beyotime Biotechnology) for 10 min, and blocked with QuickBlock blocking buffer (Beyotime Biotechnology) for 10 min at room temperature. Fourth, after washing three times with PBS, the cells were stained with anti-gamma H2AX (phospho S139) antibody [EP854(2) Y] (Abcam, dilution 1:400) at 4 °C overnight. Fifth, after washing three times with PBS, the cells were incubated with the goat polyclonal secondary antibody to rabbit IgG-H&L (Alexa Fluor® 647) (Abcam, dilution 1:400) for 1 h. Sixth, after washing three times with PBS, the cells were stained with DAPI (Beyotime Biotechnology) for 5 min. Finally, the cells were washed three times with PBS followed by the addition of 1 mL PBS. Then the fluorescence images of cells were collected by CLSM.

In vitro hemolysis assay

1 mL of fresh blood was taken from BALB/c mouse and stored in a tube containing EDTA. 2 mL of saline was added and mixed. Red blood cells (RBC) were collected by centrifuging the blood at 5000 rpm for 3 min. Then the RBC was washed three times with saline until the supernatant became colorless. After discarding the supernatant, 100 μL of RBC was taken and redispersed into 5 mL saline to prepare 2% volume fraction RBC suspension. Then a series of mixtures were prepared by mixing 500 μL RBC suspension and 500 μL saline containing Au@Cu_{2-x}Se with different concentrations. The final concentrations of Au@Cu_{2-x}Se in the mixtures were set at 12.5, 25, 50, 100, and 200 $\mu\text{g mL}^{-1}$, respectively. The mixture of 500 μL RBC suspension and 500 μL saline, and the mixture of 500 μL RBC suspension and 500 μL pure water,

were used as negative and positive controls, respectively. After remaining stable at room temperature for 5 h, these mixtures were centrifuged at 15,000 rpm for 15 min. Finally, the absorbance (A) of supernatant in different mixtures was recorded at 570 nm on microplate reader for calculating the hemolysis rate of RBC. Hemolysis rate was calculated according to Eq. 5.

$$\text{Hemolysis rate} = \frac{A_{\text{sample}} - A_{\text{saline}}}{A_{\text{H}_2\text{O}} - A_{\text{saline}}} \times 100\% \quad (5)$$

In vivo toxicity

After 200 μL of saline (control group) or 200 μL of Au@Cu_{2-x}Se suspended in saline (2 mg mL^{-1}) were injected into mice via intravenous injection ($n = 3$, per group), mice were sacrificed at 14 d to collect blood for hematological analyses and tissues (including heart, liver, spleen, lung, and kidney) for H&E stain. In these 14 days, weights of mice were measured every 2 days.

Tumor model

100 μL PBS containing 4T1.2 cells (2×10^6 cells mL^{-1}) was subcutaneously injected beside the foreleg of a BALB/c female mouse (6-weeks old). When tumor grows to $\sim 80 \text{ cm}^3$, the tumor-bearing mouse was used in subsequent in vivo experiments.

In vitro and in vivo PA imaging

PA imaging was performed on an ultrasound-photoacoustic dual-mode imaging system (VEVO LAZR-X, Fujifilm VisualSonics). The excitation wavelength for PA imaging was 808 nm. For in vitro PA imaging, various Au@Cu_{2-x}Se aqueous dispersions with concentrations of 0, 25, 50, 100, and 200 $\mu\text{g mL}^{-1}$ were injected into polyethylene tubes for PA testing, respectively. For in vivo PA imaging, 200 μL saline containing Au@Cu_{2-x}Se NPs (2 mg mL^{-1}) were intravenously injected into tumor-bearing mice ($n = 3$). Then the ultrasound and photoacoustic signals at tumor site were recorded at 1, 2, 4, 6, and 8 h post-injection, respectively. The signals before injection were used as control.

In vitro and in vivo CT imaging

CT imaging was collected from the Siemens Inveon PET/CT imaging system. For in vitro CT imaging, various Au@Cu_{2-x}Se aqueous dispersions with concentrations of 0, 0.625, 1.25, 2.5, and 5 mg mL^{-1} were placed in small tubes for CT imaging. In vivo CT imaging was conducted with tumor-bearing mice ($n = 3$, per group) after intravenous or intratumoral injection of Au@Cu_{2-x}Se NPs. For intravenous injection, the CT images were

collected at 1, 2, 4, 6, and 8 h post-injection of 200 μL saline containing Au@Cu_{2-x}Se NPs (2 mg mL⁻¹). The CT images before injection were used as control. For intratumoral injection, the CT images were collected after injection of 150 μL saline containing Au@Cu_{2-x}Se NPs with 0, 6, and 8 mg mL⁻¹, respectively.

In vivo PTT and CDT

Tumor-bearing mice were divided randomly into five groups (n = 5, per group): (1) saline; (2) saline + NIR (1.5 W cm⁻²); (3) Au@Cu_{2-x}Se; (4) Au@Cu_{2-x}Se + NIR (1.0 W cm⁻²); (5) Au@Cu_{2-x}Se + NIR (1.5 W cm⁻²). Mice in group (1) and (2) were intravenously injected with 200 μL pure saline, while mice in group (3), (4), and (5) were intravenously injected with 200 μL saline containing Au@Cu_{2-x}Se NPs (2 mg mL⁻¹). At 4 h post-injection, tumors in group (2) and (5) were irradiated with 808 nm NIR laser for 5 min at 1.5 W cm⁻², while tumors in group (4) were irradiated with 808 nm NIR laser for 5 min at 1.0 W cm⁻². The temperature changes at tumor sites were recorded with a thermal camera. The length and width of tumors and weight of mice were measured every 2 days. The tumor volume (V) was calculated according to equation $V = (\text{width}^2 \times \text{length})/2$. The relative tumor volume (V/V₀) was obtained by normalizing the tumor volume to the initial tumor volume (V₀). Besides, the tumors at 20 h post-treatment were collected for H&E and TUNEL analyses. For in vivo ROS detection in tumor, 200 μL saline containing DCFH-DA (100 μM) was intratumorally injected into the tumor-bearing mice at 3.5 h post-injection of saline or Au@Cu_{2-x}Se NPs. 30 min later, NIR irradiation was administered. Then, tumors in each group were collected for fluorescence analysis.

Intratumoral injection of Au@Cu_{2-x}Se NPs was also carried out to evaluate synergistic therapy of PTT + CDT. Tumor-bearing mice were divided randomly into four groups (n = 5, per group): (1) saline; (2) saline + NIR; (3) Au@Cu_{2-x}Se; (4) Au@Cu_{2-x}Se + NIR. After intratumoral injection of 100 μL pure saline or 100 μL saline containing Au@Cu_{2-x}Se NPs (2 mg mL⁻¹), tumors in group (2) and (4) were then irradiated with 808 nm NIR laser for 5 min at 0.5 W cm⁻². Tumors at 20 h post-treatment were collected for H&E and TUNEL analyses.

Statistical analysis

Bars display mean \pm s.d., and statistical analysis was performed using Student's *t*-test and the *P* values were provided (***P* < 0.001; ***P* < 0.01; **P* < 0.05).

Supplementary Information

The online version contains supplementary material available at <https://doi.org/10.1186/s12951-021-01159-x>.

Additional file 1. Additional tables and figures.

Authors' contributions

LZ designed the study and wrote the manuscript; CJ, BL, and ZL collected and analyzed the data; BG, SH, and PL contributed to the methodology; YS and SS supervised the study, contributed to the resource, and reviewed the manuscript. All authors read and approved the final manuscript.

Funding

This work was financially supported by the National Natural Science Foundation of China (81771861, 81971648), the Shanghai Scientific and Technological Innovation Program (18410711200, 19142202100), the National Key Research and Development Project (SQ2019YFC160090/05), the Science and Technology Development Fund of Shanghai Pudong New Area (PKJ2020-Y55, PKJ2019-Y06), the China Postdoctoral Science Foundation (2020M670997), and the Fudan University Shanghai Cancer Center Research Project (YJQN202008, YJYX201906).

Availability of data and materials

All data generated or analyzed during this study are included in this published article and its Additional files.

Declarations

Ethics approval and consent to participate

All animal experiments were approved by the Institutional Animal Care and Use Committee of Shanghai Proton and Heavy Ion Center.

Consent for publication

All authors agreed to publish this manuscript.

Competing interests

The authors declare that they have no competing interests.

Author details

¹Department of Nuclear Medicine, Shanghai Proton and Heavy Ion Center, Fudan University Cancer Hospital, Shanghai 201321, China. ²Department of Research and Development, Shanghai Proton and Heavy Ion Center, Shanghai 201321, China. ³Shanghai Key Laboratory of Radiation Oncology (20dz2261000), Shanghai, China. ⁴Shanghai Engineering Research Center of Proton and Heavy Ion Radiation Therapy, Shanghai, China.

Received: 13 October 2021 Accepted: 22 November 2021

Published online: 07 December 2021

References

- Yang B, Chen Y, Shi J. Reactive oxygen species (ROS)-based nanomedicine. *Chem Rev.* 2019;119:4881–4985.
- Gorrini C, Harris IS, Mak TW. Modulation of oxidative stress as an anticancer strategy. *Nat Rev Drug Discov.* 2013;12:931–47.
- Zhang C, Wang X, Du J, Gu Z, Zhao Y. Reactive oxygen species-regulating strategies based on nanomaterials for disease treatment. *Adv Sci.* 2020;8:2002797.
- Tang Z, Zhao P, Wang H, Liu Y, Bu W. Biomedicine meets Fenton chemistry. *Chem Rev.* 2021;121:1981–2019.
- Tang Z, Liu Y, He M, Bu W. Chemodynamic therapy: tumor microenvironment-mediated Fenton and Fenton-like reactions. *Angew Chem Int Ed.* 2019;58:946–956.
- Gao S, Lin H, Zhang H, Yao H, Chen Y, Shi J. Nanocatalytic tumor therapy by biomimetic dual inorganic nanozyme-catalyzed cascade reaction. *Adv Sci.* 2019;6:1801733.

7. Liu Y, Zhen W, Wang Y, Liu J, Jin L, Zhang T, Zhang S, Zhao Y, Song S, Li C, Zhu J, Yang Y, Zhang H. One-dimensional Fe₂P acts as a Fenton agent in response to NIR II light and ultrasound for deep tumor synergetic theranostics. *Angew Chem Int Ed*. 2019;58:2407–2412.
8. Zhang Q, Guo Q, Chen Q, Zhao X, Pennycook SJ, Chen H. Highly efficient 2D NIR-II photothermal agent with Fenton catalytic activity for cancer synergistic photothermal-chemodynamic therapy. *Adv Sci*. 2020;7:1902576.
9. Ma B, Wang S, Liu F, Zhang S, Duan J, Li Z, Kong Y, Sang Y, Liu H, Bu W, Li L. Self-assembled copper–amino acid nanoparticles for in situ glutathione “AND” H₂O₂ sequentially triggered chemodynamic therapy. *J Am Chem Soc*. 2018;141:849–857.
10. Liu X, Zhang M, Yan D, Deng G, Wang Q, Li C, Zhao Z, Lu J. A smart theranostic agent based on Fe-HPPy@Au/DOX for CT imaging and PTT/chemotherapy/CDT combined anticancer therapy. *Biomater Sci*. 2020;8:4067–4072.
11. Ruan J, Liu H, Chen B, Wang F, Wang W, Zha Z, Qian H, Miao Z, Sun J, Tian T, He Y, Wang H. Interfacially engineered Zn_xMn_{1-x}S@Polydopamine hollow nanospheres for glutathione depleting photothermally enhanced chemodynamic therapy. *ACS Nano*. 2021;15:11428–11440.
12. Ji M, Xu M, Zhang W, Yang Z, Huang L, Liu J, Zhang Y, Gu L, Yu Y, Hao W, An P, Zheng L, Zhu H, Zhang J. Structurally well-defined Au@Cu_{2-x}S core-shell nanocrystals for improved cancer treatment based on enhanced photothermal efficiency. *Adv Mater*. 2016;28:3094–101.
13. Ding X, Liow CH, Zhang M, Huang R, Li C, Shen H, Liu M, Zou Y, Gao N, Zhang Z, Li Y, Wang Q, Li S, Jiang J. Surface plasmon resonance enhanced light absorption and photothermal therapy in the second near-infrared window. *J Am Chem Soc*. 2014;136:15684–93.
14. Muhammed MA, Doblinger M, Rodriguez-Fernandez J. Switching plasmons: gold nanorod-copper chalcogenide core-shell nanoparticle clusters with selectable metal/semiconductor NIR plasmon resonances. *J Am Chem Soc*. 2015;137:11666–11677.
15. Zhang L, Mao F, Zheng LR, Wang FH, Yang XH, Yang HG. Tuning metal catalyst with metal–C₃N₄ interaction for efficient CO₂ electroreduction. *ACS Catal*. 2018; 8:11035–11041.
16. Chen XQ, Li Z, Dou SX. Ambient facile synthesis of gram-scale copper selenide nanostructures from commercial copper and selenium powder. *ACS Appl Mater Interfaces*. 2015;7:13295–302.
17. Zhang C, Yan L, Wang X, Dong X, Zhou R, Gu Z, Zhao Y. Tumor microenvironment-responsive Cu₂(OH)PO₄ nanocrystals for selective and controllable radiosensitization via the X-ray-triggered Fenton-like reaction. *Nano Lett*. 2019;19:1749–1757.
18. Zhou R, Liu X, Wu Y, Xiang H, Cao J, Li Y, Yin W, Zu Y, Li J, Liu R, Zhao F, Liu Z, Chen C, Gu Z, Yan L, Zhao Y. Suppressing the radiation-induced corrosion of bismuth nanoparticles for enhanced synergistic cancer radiophototherapy. *ACS Nano*. 2020;14:13016–13029.
19. Kang S, Gil YG, Min DH, Jang H. Nonrecurring circuit nanozymatic enhancement of hypoxic pancreatic cancer phototherapy using speckled Ru-Te hollow nanorods. *ACS Nano*. 2020;14:4383–4394.
20. Ju Y, Zhang H, Yu J, Tong S, Tian N, Wang Z, Wang X, Su X, Chu X, Lin J, Ding Y, Li G, Sheng F, Hou Y. Monodisperse Au-Fe₂C janus nanoparticles: an attractive multifunctional material for triple-modal imaging-guided tumor photothermal therapy. *ACS Nano*. 2017;11:9239–9248.
21. Lei P, An R, Zhang P, Yao S, Song S, Dong L, Xu X, Du K, Feng J, Zhang H. Ultrafast synthesis of ultrasmall poly(vinylpyrrolidone)-protected bismuth nanodots as a multifunctional theranostic agent for in vivo dual-modal CT/photothermal-imaging-guided photothermal therapy. *Adv Funct Mater*. 2017;27:1702018.
22. Zada S, Dai W, Kai Z, Lu H, Meng X, Zhang Y, Cheng Y, Yan F, Fu P, Zhang X, Dong H. Algae extraction controllable delamination of vanadium carbide nanosheets with enhanced near-infrared photothermal performance. *Angew Chem Int Ed*. 2020;59:6601–6606.
23. Miao Z, Huang D, Wang Y, Li WJ, Fan L, Wang J, Ma Y, Zhao Q, Zha Z. Safe-by-design exfoliation of niobium diselenide atomic crystals as a theory-oriented 2D nanoagent from anti-inflammation to antitumor. *Adv Funct Mater*. 2020;30:2001593.
24. Chen Q, Luo Y, Du W, Liu Z, Zhang S, Yang J, Yao H, Liu T, Ma M, Chen, H. Clearable theranostic platform with a pH-independent chemodynamic therapy enhancement strategy for synergetic photothermal tumor therapy. *ACS Appl Mater Interfaces*. 2019;11:18133–18144.
25. Huo M, Wang L, Wang Y, Chen Y, Shi J. Nanocatalytic tumor therapy by single-atom catalysts. *ACS Nano*. 2019;13:2643–2653.
26. Solier S, Pommier Y. The nuclear gamma-H2AX apoptotic ring: implications for cancers and autoimmune diseases. *Cell Mol Life Sci*. 2014;71:2289–2297.
27. Wang T, Zhang H, Liu H, Yuan Q, Ren F, Han Y, Sun Q, Li Z, Gao M. Boosting H₂O₂-guided chemodynamic therapy of cancer by enhancing reaction kinetics through versatile biomimetic Fenton nanocatalysts and the second near-infrared light irradiation. *Adv Funct Mater*. 2019;30:1906128.
28. Li ZH, Chen Y, Sun Y, Zhang XZ. Platinum-doped prussian blue nanozymes for multiwavelength bioimaging guided photothermal therapy of tumor and anti-inflammation. *ACS Nano*. 2019;13:5189–5200.

Publisher's Note

Springer Nature remains neutral with regard to jurisdictional claims in published maps and institutional affiliations.

Ready to submit your research? Choose BMC and benefit from:

- fast, convenient online submission
- thorough peer review by experienced researchers in your field
- rapid publication on acceptance
- support for research data, including large and complex data types
- gold Open Access which fosters wider collaboration and increased citations
- maximum visibility for your research: over 100M website views per year

At BMC, research is always in progress.

Learn more biomedcentral.com/submissions

